

Brain Tumor Detection Based on a Novel and High-Quality Prediction of the Tumor Pixel Distributions

Yanming Sun and Chunyan Wang

Department of Electrical and Computer Engineering, Concordia University,

1455 De Maisonneuve Blvd. W. Montreal, Quebec, Canada, H3G 1M8

Corresponding author: Chunyan Wang (chunyan@ece.concordia.ca)

Abstract

The work presented in this paper is in the area of brain tumor detection. We propose a fast detection system with 3D MRI scans of Flair modality. It performs 2 functions, predicting the gray level distribution and location distribution of the pixels in the tumor regions and generating tumor masks with pixel-wise precision. To facilitate 3D data analysis and processing, we introduce a 2D histogram presentation encompassing the gray-level distribution and pixel-location distribution of a 3D object. In the proposed system, specific 2D histograms highlighting tumor-related features are established by exploiting the left-right asymmetry of a brain structure. A modulation function, generated from the input data of each patient case, is applied to the 2D histograms to transform them into coarsely or finely predicted distributions of tumor pixels. The prediction result helps to identify/remove tumor-free slices. The prediction and removal operations are performed to the axial, coronal and sagittal slice series of a brain image, transforming it into a 3D minimum bounding box of its tumor region. The bounding box is utilized to finalize the prediction and generate a 3D tumor mask. The proposed system has been tested extensively with the data of more than 1200 patient cases in BraTS2018~2021 datasets. The test results demonstrate that the predicted 2D histograms resemble closely the true ones. The system delivers also very good tumor detection results, comparable to those of state-of-the-art CNN systems with mono-modality inputs. They are reproducible and obtained at an extremely low computation cost and without need for training.

Keywords: Brain tumor detection, Image processing, 3D MRI brain image processing, Deterministic model, Prediction of object-pixel distribution, Tumor mask generation

1. Introduction

Brain tumor detection is important for brain cancer diagnosis. As tumors can grow everywhere in the 3D space of a brain and appear in very different sizes, shapes and texture patterns, as 2 examples illustrated in Fig. 1, it is a difficult task to detect them. Hence, the analysis of brain images, such as those acquired by magnetic resonance imaging (MRI), for tumor detection is usually performed by highly-trained medical professionals, by carefully examining 3D brain images and precisely segmenting tumor regions from the images. If the resources of trained professionals are limited, the detection and diagnosis can be delayed. Developing computer vision systems for fully automatic brain tumor detection can help to reduce the work load of the medical specialists in order to improve the chance of timely diagnosis and treatments.

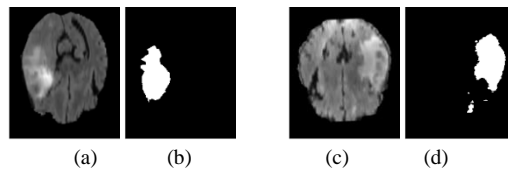


Fig. 1 (a)(c) Slices sampled from two 3D MRI brain images of Flair modality. (b)(d) Binary tumor masks of the slices in (a) and (c).

Convolutional neural network (CNN) can be considered to handle the complexity of brain tumor detection, as it can have many filtering layers and a very large number of filters in each layer to deal with enormous variations in its objects. Various CNN structures have been developed for particular kinds of tasks. For example, Visual Geometry Group Net (VGG Net) [1] is used to extract various image features, and many CNNs for medical image processing are built on the basis of U-Net structure [2-3]. The processing power of a CNN is related to its number of parameters in the filtering kernels, and the values of these parameters are determined by means of a training process. It should, however, be noted that the quantity and quality of data samples should match the number of the parameters to train the CNN decently. If one attempts to have more processing power by increasing the number of kernels/parameters of a CNN, more data samples will be needed whereas the currently available data resources may not necessarily meet the growing needs. Hence, the problem of insufficient data samples is yet to be overcome one way or another.

It should also be noted that operating a CNN requires a large amount of computation, let alone training it. Though the computation capacity is constantly getting improved in recently years, the pace of growing may not

match what is desired. Moreover, the accessibility of the existing computation resources is another issue. Hence, maximizing the computation efficiency, i.e., performing the same task while using the minimum amount of computation, should still be a point drawing the attention of designers.

In contrast to CNN, conventional filtering systems are developed with little dependency on training samples and at little computation cost with respect to that required by a CNN. A good number of such systems have been reported for brain tumor detection. In general, such a system performs 2 functions, feature extraction from the input data and classification operation applied to the extracted features. As the 2 functions can be performed in different ways, there are varieties systems reported in this topic area and relevant to the work presented in this paper.

Feature extraction can be performed by means of filters. Gabor filters are commonly used for texture analysis and feature extraction in non-CNN systems. The extracted features are then applied to various classifiers. For example, the method of Extremely Randomized Trees can be used for this purpose [4,5]. In some systems, Gabor filtering method is combined with Support Vector Machine (SVM) to detect brain tumors [6,7]. One can also combine Gabor filtering and K-means clustering methods for feature extraction and SVM together with Random Forest (RF) for classification to improve the detection result [8]. Gabor filtering and Walsh-Hadamard transform (WHT) can be used for feature extraction, and Fuzzy C-Means clustering for classification [9].

Some region-based image segmentation methods are used to detect brain tumor, e.g., homogeneity- and object-feature based Random Walks (HORW) [10], and multi-agent adaptive region grow [11]. In these methods, initial seed points should be selected, and the neighboring pixels are examined and determined whether they belong to the same region of the seed.

The feature information concerning brain tumors can also be extracted by measuring asymmetry of a brain structure, as a tumor can make its left-right halves less symmetrical. The degree of asymmetry can be measured by calculating, for example, the pixel-by-pixel difference of the two 3D halves. Then, the 3D data resulting from such a calculation are used as feature data to be applied to a classifier of Random Forest [12].

It should be noted that the 3D data produced by the dissimilarity measures represent all the asymmetry caused not only by the tumors but also by the differences of texture details in healthy parts. To make the latter less pronounced, one can measure the degree of asymmetry of the 2 halves based on their statistical presentations, e.g., gray level distributions, instead of their 3D data. For example, the difference between the gray level histograms of the normal hemisphere and the pathological hemisphere of a brain are calculated by a very simple subtraction operation [13]. One can also generate multiple pairs of histograms, each of which given by 2 subregions located symmetrically in the 2 halves, and calculate the degree of dissimilarity by Bhattacharya coefficient method to find the likely tumor location [14]. By these measures, the dissimilarity of healthy parts in image details may be less pronounced, but it can still be more visible than that caused by tumors.

Due to enormous variations in brain tumor regions, it is very difficult to achieve a high detection quality by means of conventional non-CNN filtering systems, whereas CNNs require enormous computation and data resources. If one wishes to develop a brain tumor detection system of good processing quality at a very low computation cost, the symmetrical nature of brain structure can be explored but the problem of non-tumoral asymmetry should be solved, and new methods for feature extraction and classification need to be developed.

Various image processing techniques have reported to handle different medical image problems. For example, a multi-level threshold image segmentation is used for Coronavirus Disease 2019 (COVID-19) infection diagnosis [15,16]. CNN approaches are also used in developing different systems to detect, for example, colorectal polyps in colonoscopy image [17], gastrointestinal cancers in Computed Tomography (CT) and MRI image [18], and brain tumors in MRI image [19-21].

The objective of the work presented in this paper is to develop a computation-efficient system to detect brain tumors with pixel-wise precision in MRI Flair images. The system is non-CNN-based, able to find tumor information from its input data, and no training is needed. In general, MRI scanning can be done by 4 modalities, i.e., Flair, T1, T1c and T2, resulting in four 3D images, and tumor regions are more visible in images of Flair modality than the other 3. The proposed system uses only this modality to minimize the volume of the input data in order to achieve a fast detection in a computation resource-restricted environment. Moreover, in clinical

routine, some of the modalities can be missing, because of time constraints and/or image artifacts (such as patient motion) [22-25]. Thus, systems functioning with mono-modality images can be widely applicable with less restriction.

To achieve a high processing quality at the lowest computation cost, the new system is designed based on a new scheme: the main processing in the system is to predict, step by step, the gray level distribution and location distribution of the pixels in the tumor regions of a 3D brain image. The prediction result of each step is used to detect and to remove regions of non-interest, i.e., tumor-free regions, from the 3D image. Each removal reduces the data volume and improves the density of the tumor information, facilitating the prediction in the succeeding step. The final prediction result is then applied to the remaining 3D data to detect, by means of very simple operations, the tumor locations precisely. In the design of this system, the following ideas and methods have been proposed and implemented, as positive contributions to this topic area.

- Presentation of 2D histogram of 3D data. It encompasses the gray level distribution of the data and their locational distribution. As the pixels of a 3D image can be presented in a series of 2D slices, the 2D histogram illustrates how the pixels at a particular gray level, or in a given gray level range, are distributed over the slices.
- Histogram modulation function to attenuate the presence of tumor-free elements. It transforms a histogram representing the gray level distribution and location distribution of the elements in both tumoral and tumor-free areas to a histogram representing mainly the distributions of the tumoral elements. The modulation function is generated with the original data of each patient case so that its characteristic can adapt to the data distribution of the particular case.
- Method to interleave a step-by-step prediction of the gray level distribution and location distribution of pixels in the object regions and a multi-step detection/removal of non-object regions in a 3D image. The two interact with each other and complement to each other: the result of each prediction step is used to detect and to remove non-object regions, improving the density of the object information and benefiting the prediction in the following step.

This paper consists of 4 sections. The work concerning the proposed system is presented in Section 2 and it involves a proposed method to present 3D data distribution and a proposed scheme for brain tumor detection. Section 3 is dedicated to the presentation of the experiment results, using the patient cases in Brain Tumor Segmentation (BraTS) datasets [26]. A conclusion is presented in Section 4.

2. Proposed Design Method and Prediction/Detection System

Brain tumors are detected from 3D brain image data. In this section, we propose, first of all, a 2D histogram method to present the gray level distribution with the location information of 3D image data, and this method can be used to facilitate, in general, 3D object detections. The proposed system is presented in Subsections 2.2. It comprises the part of the prediction of the pixel distribution in the tumor regions, to which the major part of this subsection is dedicated, and the part of using the prediction results to precisely identify the tumor regions in a 3D brain image. The 2D histogram method is applied throughout the design process.

2.1 Two-D Histogram Presenting Gray-Level and Location Distributions of 3D Data

A tumor can appear in any location in a 3D brain structure and tumor regions can have various gray level distributions. The gray level distribution provides us with important statistical characters of the 3D regions, but without their locational information. In this subsection, we propose a 2D histogram presentation, bringing the locational information to the gray level distributions.

It is known that a 3D brain image can be presented as a series of axial, coronal or sagittal slices, and each slice has a gray level distribution. A 2D histogram presents collectively a series of distributions given by a series of slices, as an example shown in Fig. 2 (a). Let $H(i,j)$ denote such a histogram, the i -axis specifies the gray levels, normalized to $[0, 1]$, and the j -axis is the slice index, i.e., one of the 3 coordinates in the 3D structure.

If $j = j_o$ is given, $H(i,j_o)$ is the gray level distribution of the pixels in the j_o^{th} slice, whereas if $i = i_o$, $H(i_o,j)$ represents the locational distribution of the pixels at the gray level i_o over the slices in the series. Hence, a 2D histogram $H(i,j)$ encompasses the gray level distribution and locational distribution of the pixels.

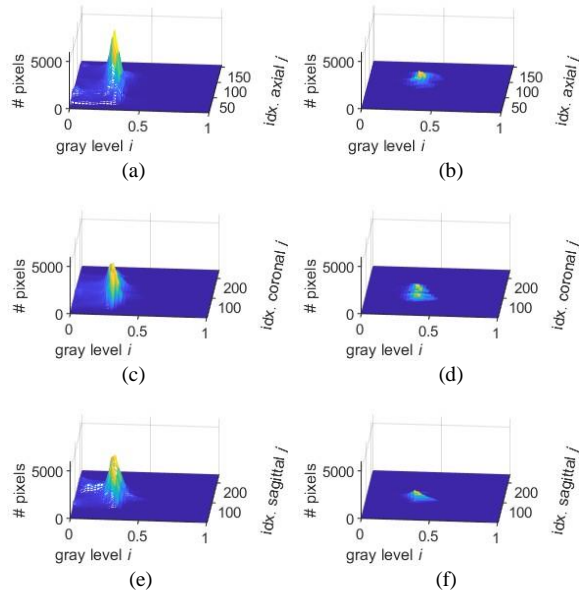


Fig. 2 Two-D histograms generated from the data of the patient case 01417 from BraTS2021 dataset. In each of them, the x-axis specifies the gray levels, normalized to $[0, 1]$, the y-axis the index of slice series, the z-axis the number of pixels. (a)(b) Two-D histograms of the 3D brain region and the tumor region given by the axial slices, (c)(d) by the coronal slices, and (e)(f) by the sagittal slices.

The 3 pairs of 2D histograms, illustrated in Fig. 2, are given by the same 3D Flair image sliced 3 times. The 2D histogram in Fig. 2 (a) is generated from the 155 axial slices and illustrates the pixel distribution of the 3D brain region, whereas Fig. 2 (b) shows that of the tumor region inside the brain. Fig. 2 (b) demonstrates that a vast majority of the tumor pixels, i.e., the pixels in the 3D tumor regions inside the brain, are found in the slices indexed 70 to 130 and approximately in the gray level range (0.25, 0.5). The coordinates in the y-axis define the location of the tumor region in the direction perpendicular to the slices. As the axial slices are indexed from the bottom up, the tumor is found in the upper part of the brain.

The 2D histogram of the tumor region in Fig. 2 (f) is given by the 240 sagittal slices of the same patient case, and presents the gray level distributions, over the slices, of the pixels in the tumor area. One can notice that the number of the slices where the tumor pixels appear is visibly smaller than that in the axial or coronal series shown in Fig. 2 (b) or (d), indicating that the tumor region is thinner in this dimension.

The three 2D histograms shown in Fig. 2 (b), (d) and (f) represent, on one hand, the three gray level distributions of the same tumor region in the three series, respectively. On the other hand, they indicate the

coordinates of the tumor location in the 3D brain image. In other words, one can find the tumor-free axial, coronal or sagittal slices, respectively, in the three 2D histograms.

It should, however, be noted that, in a real detection case, 2D histograms of tumor pixels are not available. Nevertheless, they are predictable. We propose a method to use the information from 2D histograms of a brain image to predict the gray level distribution of the tumor pixels inside the image. Based on the results of the prediction, the task of the brain tumor detection can be done easily and effectively to achieve a good processing quality. The procedure of the prediction and the detection is described in the following subsection.

2.2 Proposed System

The proposed system is designed to predict 2D histograms of the pixels in the tumor region in a 3D brain image of MRI Flair modality, and the prediction results are then used to detect brain tumor with pixel-wise precision. This subsection is organized as follows. In Subsection 2.2.1, the overview of the proposed system is presented. In Subsection 2.2.2, a method to extract tumor information by a particular measure of brain structure asymmetry is described. The data extracted by the asymmetry measure have a significantly higher tumor information density, with respect to that in the input 3D data, but need to be modulated for the prediction. A modulation function is proposed and described in Subsection 2.2.3. Three-step coarse prediction and the finalization of the tumor pixel distribution are found in Subsections 2.2.4. Subsection 2.2.5 is about the brain tumor mask generation based on the predicted 2D histograms.

2.2.1 System Overview

Of a 3D input image, the object region takes, in general, only a very small percentage of the space and thus the density of the object information is extremely low in the input data. In case of brain tumor detection and there is a thick tumor-free margin in each of the 6 sides of the 3D input. In other words, in each of the 3 series of slices, namely axial, coronal and sagittal series, only a small number of slices contains tumor pixels, and the other slices are tumor-free. However, as a tumor can be found in any place in the 3D brain, it is not easy to localize these slices in the series. Moreover, though a tumor region in a Flair image often looks brighter than its surroundings, there can be darker sub-regions in it and there is no model relating the gray level distribution

of the pixels inside the tumor space to that of the entire brain. Hence, it is very challenging task to predict the 2D histograms with good precision.

In the design of the proposed system, the 3 commonly known points are explored.

- Though the object location is unknown, some object-free regions can be localized with some certainty. One can identify/remove object-free regions in multiple steps, starting from the most obvious ones, and each step results in a higher density of object information.
- A higher object information density in the input data leads to a better processing quality.
- Since a 3D input image can be sliced three times in the three different directions, i.e., x, y, z axis, resulting in 3 different series of slices, one can design a 3-step process and each step can be performed with a different series of the same 3D data.

The processing scheme in the proposed system is shown in Fig. 3. It has 3 prediction steps interleaved with 3 cropping operations. In each step, the 3D data is sliced in one of the 3 directions, the 2D histogram of the tumor pixels of this series is predicted, and the result is then applied to crop out object-free margins, i.e., tumor-free slices. The cropped 3D data is expected to have a higher object information density, with respect to that in the preceding step, and are then used for the prediction in the following step. In this way, the prediction result can be improved step by step.

In the proposed system, the symmetrical nature of the brain image is explored to produce an asymmetry map, presented as a 2D histogram, to be used to initiate the prediction. A modulation function is generated from the input data, as shown in Fig. 3, and used to modulate the 2D histogram in each step to produce the prediction result. In the present design, the same modulation function is applied to all the 3 coarse prediction steps, and a modified version to the finalization of the prediction.

The progressive removals of tumor-free regions in the proposed scheme transforms the input 3D image into a 3D minimum bounding box, in which most of the pixels are inside the tumor region. This minimum bounding box is then used to finalize the 3 predicted 2D histograms, as shown in Fig. 3.

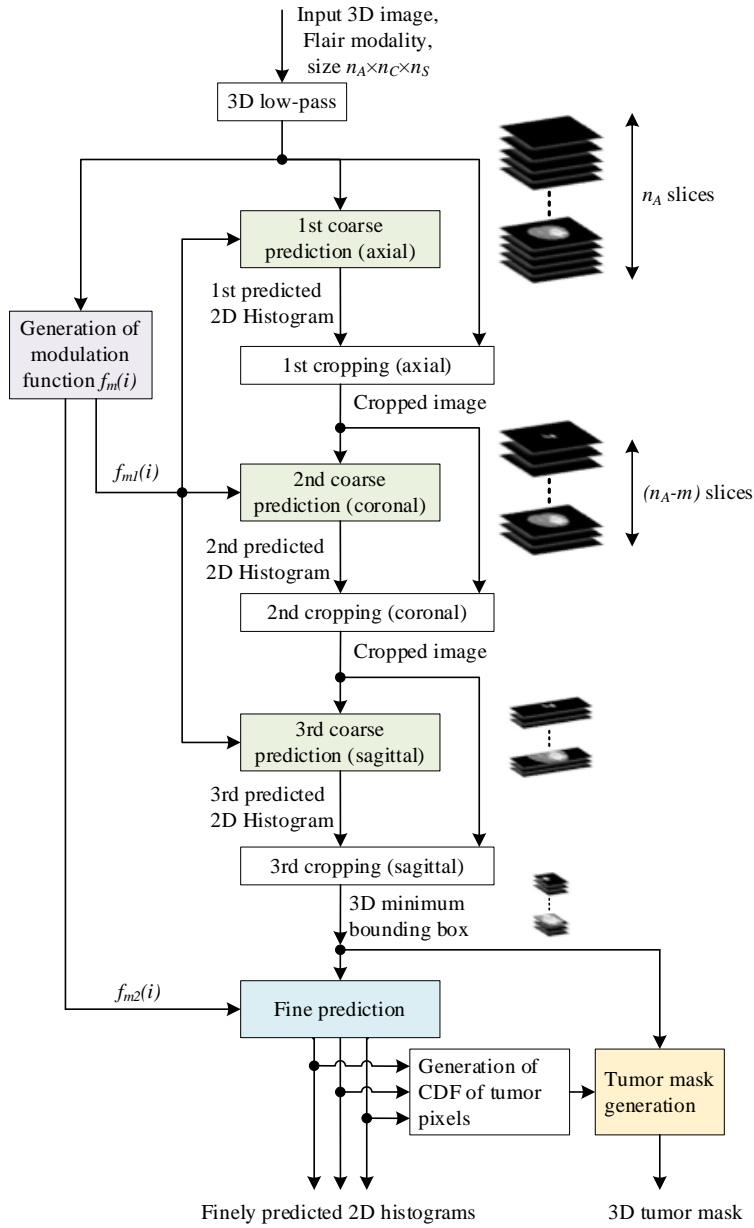


Fig. 3 Block diagram of the proposed system. It receives a 3D brain image input that can be sliced into a series of n_A axial slices, or a series of n_C coronal slices or n_S sagittal slices, and generates the predicted 2D histogram of the brain tumor region for each of the 3 series of slices and a 3D tumor mask.

The proposed system also includes a simple procedure to identify the regions of brain tumors, in which the predicted tumor pixel distributions are used to localize them in the minimum bounding box to generate a tumor mask with pixel-wise precision.

The quality of the final results is related to the data processing quality in each of the prediction steps. In particular, as the operations are performed sequentially, the first prediction and cropping are very critical. The design of the blocks is presented in the following subsections.

2.2.2 Brain Image Asymmetry Measure to Extract Tumor Information

A healthy human brain looks roughly left-right symmetrical, though its details are not really left-right mirrored [27], as an example shown in Fig. 4 (a). The presence of a brain tumor causes a more noticeable asymmetry in its structure, as shown in Fig. 4 (b) and (c). Hence, the asymmetry measures in brain images have been used to detect brain tumors [13,14,28]. It should, nevertheless, be noted that, though the tumor-related asymmetry is salient for trained human eyes, it is not prominent in an asymmetry measurement in computer vision. The results of the measurement can be more dominated by the elements representing the natural asymmetry in brain image details than those of the asymmetry caused by tumor, referred to as tumoral asymmetry.

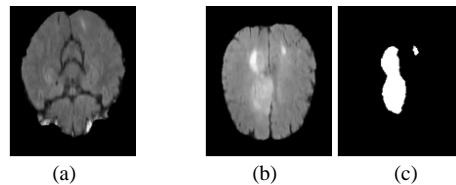


Fig. 4 (a) Slice of brain image without tumor. The left-right asymmetry in image details is referred to as natural asymmetry. (b)(c) Slice of brain image with tumor and its binary tumor mask.

The natural asymmetry in brain images is in image details, reflecting different tissues and fluid, whereas the tumoral asymmetry is more in brain structure. Before all the measures, a 3D low-pass filtering is applied to the input and then each slice is down-sampled to erase some image details so that the elements of natural asymmetry are less dominant in the asymmetry measures.

In order to make the natural asymmetry in fine image patterns less influenceable, in the proposed prediction process, the left-right asymmetry of a 3D brain image is measured simply by means of the difference between the two 2D histograms, namely $H_{left}(i,j)$ and $H_{right}(i,j)$, given by the left and right halves, respectively. It is expressed as

$$\Delta H(i,j) = |H_{left}(i,j) - H_{right}(i,j)| \quad (1)$$

where i representing the gray level, scaled between 0 and 1, and j the slice index in the axial or coronal series. As $\Delta H(i,j)$ represents the gray level distribution of the asymmetry elements over the series, it is referred to as asymmetry map.

As the gray level range of a tumor space is in an upper-level section of that of the brain region, the pixels having their gray levels below the mean level of the 3D brain region are not included in $\Delta H(i,j)$. In other words, in the asymmetry maps presented in this section, the gray scale is normalized to the range of [0,1] with $i = 0$ corresponding to the mean level of the 3D brain region.

Fig. 5 illustrates an example of $H_{left}(i,j)$, $H_{right}(i,j)$ and $\Delta H(i,j)$ obtained from a 3D Flair image of a typical patient case, in comparison with $H_T(i,j)$, the 2D histogram encompassing gray level distribution and location distribution of the true tumor region, referred to as the ground truth. Comparing $H_{left}(i,j)$ and $H_{right}(i,j)$, one can see the right half has more pixels in the upper gray levels, indicating the presence of a tumor, which is also reflected in $\Delta H(i,j)$. Comparing $\Delta H(i,j)$ and the ground truth $H_T(i,j)$, one can clearly see that the distribution in the upper level range in $\Delta H(i,j)$ is highly correlated to that of $H_T(i,j)$, but that in the lower level range is not.

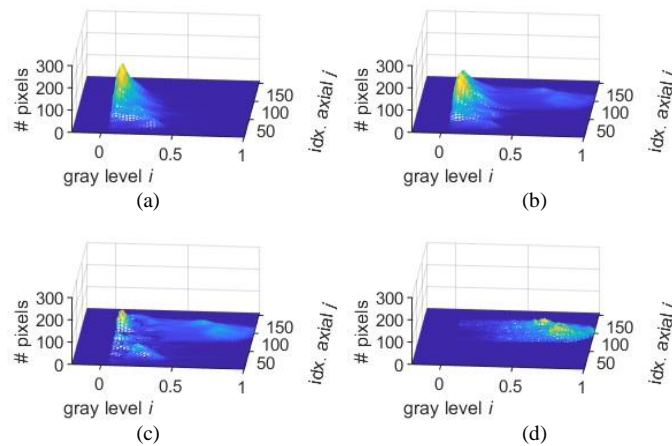


Fig. 5 Four 2D histograms obtained from the 155 axial slices of a low-passed and down-sampled 3D Flair image from Case 01412 of BraTS2021 dataset. The X-axis is the normalized gray scale and the zero point corresponds to the mean value of the 3D brain region, excluding the pixels of gray level values below the mean.
(a) $H_{left}(i,j)$, the 2D histogram of the left half of the 3D image,
(b) $H_{right}(i,j)$, the 2D histogram of the right half of the 3D image,
(c) $\Delta H(i,j) = |H_{left}(i,j) - H_{right}(i,j)|$, and (d) $H_T(i,j)$, the ground truth of the 2D gray level distribution of the tumor region.

Evidently, the upper-gray-level section of $\Delta H(i,j)$ is dominated by the pixels in the tumor region, representing more the tumoral asymmetry. The section of the lower gray levels in $\Delta H(i,j)$ is, however, more

relevant to the natural asymmetry. With a view to obtaining a good prediction of the gray level distribution of the tumor region, the data of $\Delta H(i,j)$ needs to be modulated so that the elements related to the natural asymmetry will be attenuated. The development of the modulation function is presented in the next subsection.

2.2.3 Generation of the Modulation Function

The asymmetry measurement results in a 2D histogram $\Delta H(i,j)$ representing the natural and tumoral asymmetries in the consecutive slices of a 3D brain image. The objective of the modulation is to transform $\Delta H(i,j)$ into a 2D histogram $H_m(i,j)$ resembling the true gray level distribution of the tumor pixels. In this subsection, we propose a modulation function $f_m(i)$, and $H_m(i,j)$ will simply be the product of $\Delta H(i,j) \cdot f_m(i)$.

As mentioned previously, the elements of natural asymmetry in $\Delta H(i,j)$ are found in the lower part of the gray level range, while those of tumoral asymmetry in the upper gray level part. To attenuate the former and preserve the latter, the modulation function $f_m(i)$ should be sigmoidal, i.e., being monotonic and having a bell-shaped first derivative $df_m(i)/di$. The critical point is $i = i_M$ at the peak point of $df_m(i)/di$. Based on i_M , the gray level range of $f_m(i)$ is divided into 3 sections, $i < i_M$, $i \approx i_M$ (around i_M), and $i > i_M$, with $f_m(i < i_M) \approx \min$ and $f_m(i > i_M) \approx 1$. Most of the pixels in the tumor-free regions are found in the lower gray level section of $i < i_M$, and the pixels in the mid-section of $i \approx i_M$ can be found in either tumor-free or tumor regions. Hence, the key issues in establishing $f_m(i)$ are a) to find the point of $i \approx i_M$ and b) to determine the width of the mid-section. They should match the true gray level distribution of the pixels in the tumor-free region. In the absence of such ground truth data, we need to find the information from the data of the input brain image.

In 3D brain images, since a tumor region usually appears in the left or right half, the half involving the tumor will have its histogram more populated in the upper gray levels than the other half. Let us call the first half *tumor-half* and the other *tumor-free-half*, and $h_{tumor-half}$ and $h_{tumor-free-half}$ denote their 1D histograms, respectively. Fig. 6 (a) and (b) illustrate $h_{tumor-half}$ and $h_{tumor-free-half}$ given by 2 very different patient cases, and each pair is superimposed with the ground truth $h_{tumor-free}$, the normalized gray level distribution of the pixels outside the tumor space in the entire 3D brain region. One can find, in each of these 2 cases, a high degree of similarity between $h_{tumor-free-half}$ and $h_{tumor-free}$. It indicates that, in the half that is less affected by the tumor, the

statistical characters of the data are not much different from those of the entire tumor-free regions of the brain.

Thus, $h_{\text{tumor-free-half}}$ can be used to emulate $h_{\text{tumor-free}}$ to determine the mid-section of the modulation function $f_m(i)$.

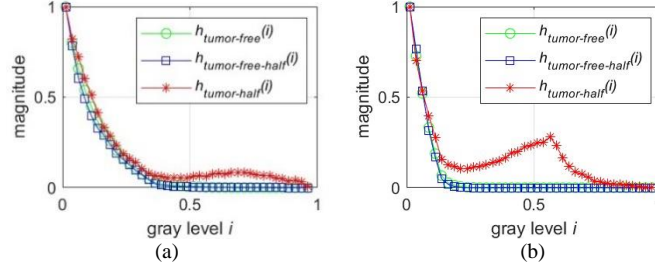


Fig. 6 Gray level distributions given by patient cases 01412 and 01414 from BraTS 2021 dataset. In the 2 graphs, $h_{\text{tumor-free-half}}$, the distribution of the pixels from the tumor-free half is compared with $h_{\text{tumor-half}}$ that of the tumor half and $h_{\text{tumor-free}}$ that of the true tumor-free region inside the entire brain region.

Of the 1251 patient cases available in BraTS2021 datasets, approximately 94% have tumors developed in either left or right half, and the above observation/analysis is valid for a vast majority of patient cases. Even though a tumor grows in the middle, its region can hardly straddle the left and right halves symmetrically. Hence, the histogram of the half having fewer tumor pixels bears a similitude of $h_{\text{tumor-free}}$ and thus can substitute it to determine $f_m(i)$.

The procedure to generate the modulation function $f_m(i)$ from the distribution of the pixels in the tumor-free half has 2 steps. The first step is to identify which of the 2 halves is more likely to be tumor-free, and the second step is to transform the distribution of the pixels of the identified half into a desired $f_m(i)$.

As the pixels in tumor regions are in the upper-gray-level section, the tumor-free half of the 3D brain image should have a smaller number of high-gray-level pixels with respect to the other half. Hence, the identification is done by simply counting the number of pixels in the upper-gray-level section. In case of samples from BraTS2021, this section is defined as $[0.55, 1]$ in the normalized gray scale, in which the point $i = 0$ corresponds to the mean value of the pixels in the brain region.

Once the tumor-free half is identified, the 1D distribution of its pixels, denoted by $h_{\text{tf}}(i)$, can be generated. Transforming $h_{\text{tf}}(i)$ into a desired $f_m(i)$ is done mainly by truncation and inversion. A block diagram of the transformation presented in Fig. 7 (a), and the curves of the data in this process is visualized in Fig. 7 (b). The

input $h_f(i)$, plotted in blue, is truncated to limit the heights of its bins, resulting in $h_T(i)$ plotted in cyan. The curve of $1/h_T(i)$, plotted in black, can be adjusted to approach the expected $f_m(i)$, plotted in magenta. In this process, low-pass filtering operations are applied before and after the inversion to remove the discontinuity in the curves. The mathematic expressions used in the transformation process are as follows.

$$h_T(i) = \begin{cases} \max_T, & h_{tf}(i) > \max_T \\ h_{tf}(i), & \min_T \leq h_{tf}(i) \leq \max_T \\ \min_T, & h_{tf}(i) < \min_T \end{cases} \quad (2)$$

$$f_m(i) = \left[\frac{1}{h_T(i)} \right]^\gamma + \alpha \quad (3)$$

where \max_T and \min_T are the pre-determined highest and lowest bin-heights, γ is a correction factor, and α is a constant.

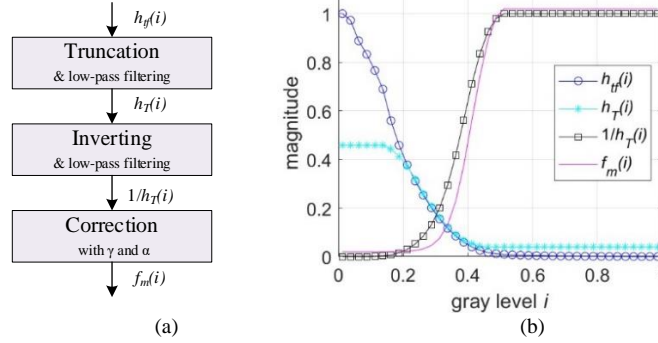


Fig. 7 (a) Block diagram of the procedure to transform $h_f(i)$ to $f_m(i)$. (b) Graph of $h_f(i)$ of a 3D Flair image, $h_T(i)$, truncated $h_f(i)$ with $\max_T \approx 0.5$, $\min_T \approx 0.05$, $1/h_T(i)$ and $f_m(i)$ given by Eq. (3) with $\gamma = 1.8$ and $\alpha = 0.02$.

The modulation function $f_m(i)$ can be fine-tune by means of the four parameters, \max_T and \min_T , γ , and α . One can use \max_T and \min_T to fine-tune, respectively, the 2 particular points where $df_m(i)/di = 1$, and these 2 points define mid-section of $f_m(i)$ curve. The parameter γ can be used to modify $df_m(i)/di$ in this section, and $\alpha \ll 1$ to maintain a minimum value of $f_m(i)$. For example, increasing the values of \max_T and \min_T shifts the mid-section slightly left-wards, making the modulation "milder", i.e., attenuating less the elements in mid gray level range.

In summary, the modulation function $f_m(i)$ is generated from the input data of each patient case and it is able to adapt to the distributions of individual cases. Its effectiveness in attenuating the element irrelevant to

the tumor regions, while preserving those relevant to the tumors, will be confirmed in the design and test of the proposed system presented in the following subsections.

2.2.4 Prediction of the Tumor Pixel Distribution

The core of the proposed system is the procedure of 3 coarse predictions of the 2D histograms of the tumor pixels interleaved with 3 cropping operations, as shown in Fig. 3. The 3 coarse predictions are performed with axial, coronal and sagittal slice series, respectively. The objective of each prediction is to find the concentration of likely tumor pixels in order to identify the likely tumor-free slices that are then removed, i.e., cropped out, from the slice series.

The processing in the first 2 steps are performed with the axial and coronal slices, respectively, as each of them reflects the left-right symmetry of brain structure, allowing to generate an asymmetry map $\Delta H(i,j)$, whereas that in the third step is with a series of cropped sagittal slices. After the 3-step prediction and cropping, the input 3D image is reduced to a minimum bounding box, from which the predicted distribution of the tumor region is refined. The details of the prediction and cropping operations are presented in the following subsections.

2.2.4.1 First Two Coarse Predictions and Cropping Operations

In the proposed system, the first coarse prediction is performed on the axial slices. Let $\Delta H_a(i,j)$ denote the asymmetry map generated from the axial slices and $H_{ma}(i,j)$ denote the coarsely predicted distribution of the tumor pixels over the axial slices, we have $H_{ma}(i,j) = \Delta H_a(i,j) \cdot f_{ml}(i)$. The modulation function $f_{ml}(i)$ is defined by Eqs. (2) and (3), described in Subsection 2.2.3, generated from the data of the tumor-free half of the original 3D input.

The modulated 2D histogram $H_{ma}(i,j)$ represents the asymmetry in the upper gray levels, where most of the pixels in the tumor region are found. Thus, it is highly correlated with $H_{Ta}(i,j)$, the 2D histogram of the pixels in the tumor region given by the ground truth.

Fig. 8 (a) and (b) illustrates an example of the first prediction results, in which $\Delta H_a(i,j)$ and $H_{ma}(i,j)$ are obtained from the same patient case shown in Fig. 5. Comparing $H_{ma}(i,j)$ with $H_{Ta}(i,j)$ shown in Fig. 8 (c), one can observe that 1) $H_{ma}(i,j)$ emulates well the distribution of most pixels in the tumor region and 2) it indicates a slice-index range, very similar to that in $H_{Ta}(i,j)$, where the tumor pixels are located. The same degree of similarity is also observed in the prediction results of a vast majority of the 1251 patient cases in BraTS2021 dataset. Thus, in the absence of $H_{Ta}(i,j)$, $H_{ma}(i,j)$ can be considered as a coarsely predicted 2D histogram of the tumor pixels in the consecutive axial slices.

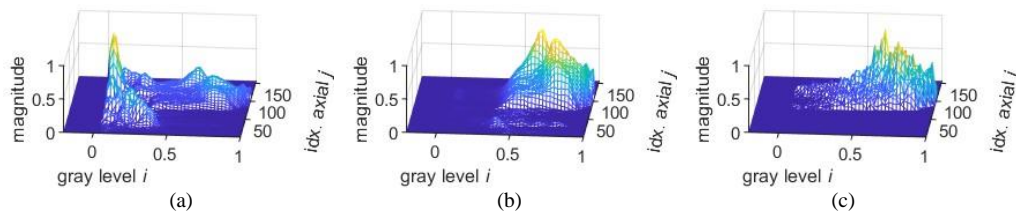


Fig. 8 (a) Asymmetry map $\Delta H_a(i,j)$, generated with the axial slice series of the patient case 01412 from BraTS2021 dataset. (b) Modulated 2D histogram of the axial slice series, $H_{ma}(i,j)$, to be used as a coarsely predicted 2D histogram of the tumor region. (c) True 2D histogram of the tumor pixels, $H_{Ta}(i,j)$, over the axial slices.

To identify the tumor-free axial slices, we have $h_{La}(j) = \sum_i H_{ma}(i,j)$ representing the locational distribution of the tumor pixels in the axial slice. An example of $h_{La}(j)$ shown in Fig. 9 (b) is obtained from $H_{ma}(i,j)$ shown in Fig. 9 (a). High magnitudes in $h_{La}(j)$ indicate the concentration of pixels of interest, i.e., tumor pixels, in the corresponding slices. The index range of these slices is determined by the two local minima in $h_{La}(j)$ curve. The slices indexed between them are considered slices with tumor, and the others tumor-free. One can see in Fig. 9 (b) that the set of the axial slices identified as tumor slices are almost identical to that in the ground truth. The tumor-free slices, found on the top and bottom of the input 3D image, constitute two tumor-free margins and are then effectively cropped out.

By the first cropping operation, the size of the 3D image is reduced significantly. Of the 1251 patient cases in BraTS2021, it results in a removal of more than 60% axial slices from the 3D brain region, while losing only less than 4% of the tumor pixels.

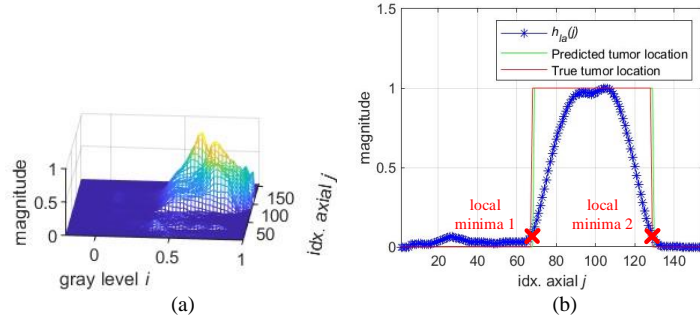


Fig. 9 (a) Coarsely predicted 2D histogram of the tumor region, $H_{ma}(i,j)$, over a series of axial slices. (b) Predicted locational distribution of the tumor pixels over the series of axial slices, $h_{La}(j)$, plotted in blue. The 2 local minima define the 2 boundaries of the predicted set of consecutive tumor slices, specified by the green frame, in comparison with the ground truth framed in red. The data sample is from the patient case 01412 of BraTS2021.

The second coarse prediction is then applied to the cropped 3D image presented as a series of coronal slices. The number of slices in this series is the same as that of the original Flair image, but the number of non-zero pixels per slice is much smaller because the predicted tumor-free top and bottom margins of the input 3D image have been cropped out in the first step of prediction/cropping, as examples shown in Fig. 10. Nevertheless, the overall left-right symmetry is preserved in the tumor-free coronal slices, and a coronal asymmetry map $\Delta H_c(i,j)$ can be generated to represent the distribution of asymmetrical elements from the cropped coronal slices.

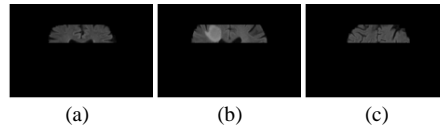


Fig. 10 Coronal slices sampled from a 3D image, after the tumor-free axial slices are removed in the first cropping. (a)(c) Cropped coronal slice without tumor and (b) that with tumor. The left-right asymmetry in (b) is much more noticeable than that in (a) or (c).

The procedure of the second prediction is the same as the first one. The same modulation function $f_{m1}(i)$ is applied to the coronal asymmetry map $\Delta H_c(i,j)$ obtained from the coronal slices to generate the second predicted tumor pixel distribution $H_{mc}(i,j)$.

The cropping operation following the second coarse prediction is identical to that in the first step, resulting in the removal of 2 sets of coronal slices that are considered tumor-free. At that point, the predicted tumor-free margins in the top, bottom, back and front sides of the original 3D input have been cropped out. Fig. 11 illustrates a few examples of cropped sagittal slices, in comparison with the original ones. The series of such sagittal slices is then ready for the next step of prediction and cropping.

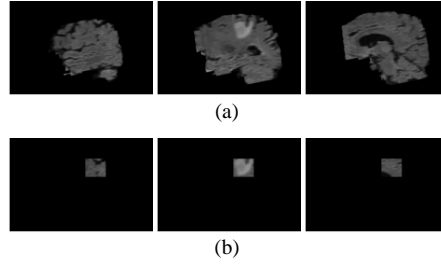


Fig. 11 Sagittal slices samples (a) before the 2 cropping operations, (b) after the cropping operations applied to the axial and coronal slices. The slice in the center involves a tumor region and the other 2 are tumor-free.

2.2.4.2 Third Coarse Prediction & Cropping and the Final Prediction

The objective of the 3rd coarse prediction and cropping is to identify tumor-free sagittal slices and to remove them. As a sagittal slice does not feature left-right symmetry, no asymmetry map can be generated in this step. It should, however, be noted that the percentage of tumor pixels in this sagittal slice series is evidently much higher than that of the original 3D input. The prediction in this 3rd step is done by modulating $H_s(i,j)$, the 2D histogram of a sagittal series of a 3D brain image already cropped twice. The coarsely predicted 2D histogram of the tumor pixels over the sagittal slices is denoted as $H_{ms}(i,j) = H_s(i,j) \cdot f_{m1}(i)$, with the same $f_{m1}(i)$ used in the 2 previous coarse prediction steps. Similar to the modulations in the 2 previous steps, the elements in the lower-gray-level section of $H_s(i,j)$ are attenuated, resulting in $H_{ms}(i,j)$ resembling the true 2D histogram of the tumor pixels over the sagittal slices.

The cropping operation in this step is identical to that in the other steps. It results in the removal of the 2 sets of tumor-free sagittal slices, i.e., the tumor-free margins in the left and right sides of the 3D input. By the 3-step cropping, the original 3D input is reduced to a 3D minimum bounding box, in which most of the pixels are found in the tumor region.

The operation of the fine prediction is applied to the data of the 3D minimum bounding box. Its axial, coronal and sagittal slice series give three 2D histograms, denoted by $H_{ba}(i,j)$, $H_{bc}(i,j)$ and $H_{bs}(i,j)$, respectively. An example is illustrated in Fig. 12 (a) (d) and (g). Comparing the 3 histograms with the ground truth of the tumor pixel distributions illustrated in Fig. 12 (c) (f) and (i), one can notice that 1) the 2 sets are very similar in the upper-gray-level section and 2) their differences are found in the lower and mid gray level sections, as the minimum bounding box involves tumor-free regions. Hence, like the coarse predictions, the operation for the

fine prediction is to attenuate the elements of $H_{ba}(i,j)$, $H_{bc}(i,j)$ and $H_{bs}(i,j)$ in the mid and lower-gray-level sections by a simple modulation.

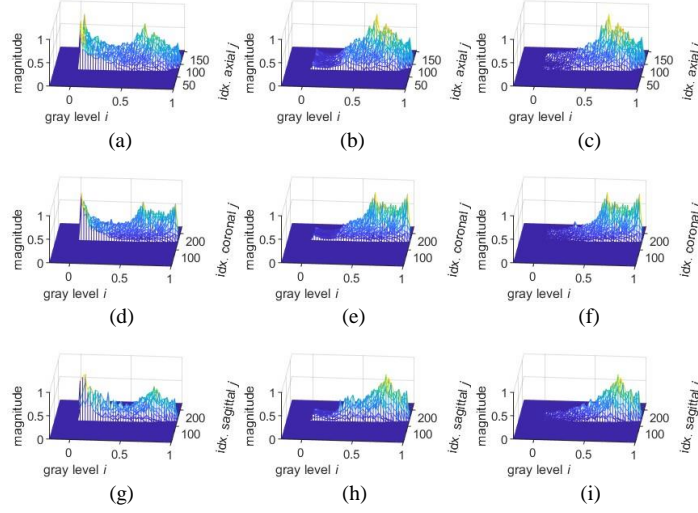


Fig. 12 (a)(d)(g) Two-D histograms of the axial, coronal and sagittal slice series given by the minimum bounding box. (b)(e)(h) Predicted 2D histograms of tumor pixels in the axial, coronal and sagittal slice series. (c)(f)(i) Ground truth of the 2D histograms in (b)(e)(h). The data sample is from the patient case 01412 in BraTS2021.

It should, however, be noticed that the gray levels of the pixels in tumor regions can cover a wide range. Though a majority of the tumor pixels is found in the upper-gray-level section, a non-negligible minority is found in the mid and lower sections, which should be taken into consideration in the fine prediction. Hence, the modulation function in this stage is adjusted to attenuate less elements in the mid and lower gray-level ranges, with respect to that in the coarse prediction steps.

The final prediction results in the three 2D histograms, denoted as $H_{pa}(i,j)$, $H_{pc}(i,j)$ and $H_{ps}(i,j)$, indicating the gray level distribution of the tumor pixels over the axial, coronal, and sagittal slice series, respectively. They are expressed as follows.

$$\begin{cases} H_{pa}(i,j) = H_{ba}(i,j) \cdot f_{m2}(i) \\ H_{pc}(i,j) = H_{bc}(i,j) \cdot f_{m2}(i) \\ H_{ps}(i,j) = H_{bs}(i,j) \cdot f_{m2}(i) \end{cases} \quad (4)$$

where $f_{m2}(i)$ is defined by Eqs. (2) and (3). Compared to $f_{m1}(i)$, the characteristic of f_{m2} is slightly left-wards shifted, the slope, $df_{m2}(i)/di$, in mid-section is gentler, and the minimum value of $f_{m2}(i)$ is increased to preserve

more pixels in the lower and mid gray-level range. It is done by i) slightly increasing max_T and min_T , ii) reducing γ and iii) increasing α .

An example of the 3 predicted 2D histograms are presented in Fig. 12 (b)(e)(h). The ground truth data of the tumor distributions are presented in Fig. 12 (c)(f)(i). One can find that, the predicted tumor distributions are very similar to the ground truth. They can be used, for example, to detect the whole tumor regions with pixel-wise precision in the brain image.

2.2.5 Brain Tumor Mask Generation

In the proposed system, illustrated in Fig. 3, the input data of the block labeled “Tumor mask generation”, is the 3D bounding box after the 6 tumor-free margins are cropped out from an original 3D brain image of Flair modality. The gray level distribution of the tumor pixels has been predicted, but their precise locations in this bounding box are not specified. The processing in this detection block is to transform the bounding box into a 3D binary tumor mask with pixel-wise precision. The transformation is done by 2 very simple operations, i.e., pixel binarization by gray level thresholding and morphological process by low-pass filtering.

The binarization is to divide, coarsely by a simple gray level thresholding, the pixels in the bounding box into 2 groups, those inside the tumor region and those outside. The threshold should be determined with 2 issues taken into consideration.

- It should adapt to the gray level distribution of the pixels in each individual case.
- The gray level range of the pixels in the tumor region can overlap completely that of the tumor-free regions, as the example shown in Fig. 13 (a). The threshold is determined in such a way that most of the tumor-free pixels are put in one side and most of tumor pixels on the other side, resulting in unavoidably a misplacement of a minority of the pixels in each side.

In practice, it is reasonable to allow, e.g., 20% of tumor pixels to be misplaced if their misplacement is insignificant enough to be corrected in the following processing. In this case, the threshold is found at the gray level point corresponding to 20% in the cumulative distribution function (CDF) of the tumor pixel population, as shown in Fig. 13 (b). The thresholds defined in this manner can be adaptive to the various distributions of

individual cases. Since the true distribution of the tumor area is not available, the predicted one is used to determine the threshold.

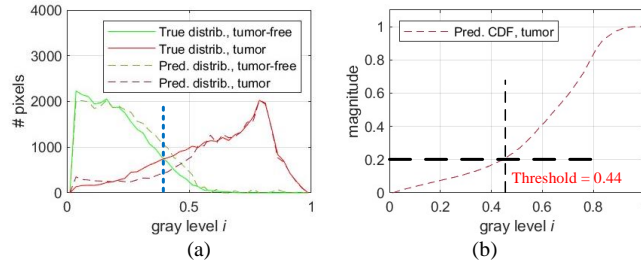


Fig. 13 (a) Gray level distributions of the tumoral or tumor-free pixels in a 3D minimum bounding box. The solid curves are given by the ground truth, and the dashed curves by the predicted distributions. The blue dashed line indicates an assumed gray level threshold. (b) CDF derived from the predicted distribution of the tumor pixels. The point of CDF = 20% determines the gray level threshold of 0.44 in this patient case.

The binarization by means of a simple thresholding results in a coarse binary tumor mask with a minority of the pixels misplaced. A slice of such a 3D mask is illustrated in Fig. 14 (b). To correct the misplacement, a morphological operation is applied. In this design, it is done by (i) a convolution with a simple 3D averaging kernel of $5 \times 5 \times 5$ pixels and (ii) assigning the logic-1 value to all the pixels having their gray levels greater than a pre-determined floor and logic-0 to the others. Fig. 14 (c) illustrates the slice generated by such a morphological operation, in comparison with the ground truth illustrated in Fig. 14 (d).

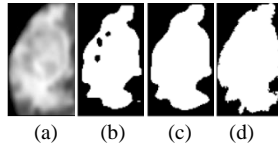


Fig. 14 (a) Slice from a 3D minimum bounding box generated from the data of the patient case 01418 of BraTS2021 dataset. (b) Slice of the coarse mask after the binarization. (c) Slice of the final binary mask after the morphological operation. (d) Slice of the true tumor mask.

This tumor mask generation is done by the 2 very simple operations, as it is performed on the data of the predicted 3D minimum bounding boxes of tumors and the predicted tumor pixel distribution. Hence it is an application of the prediction results, and the quality of the operations depends very much on the quality of the prediction. Various quality measures have been conducted to evaluate the performance of the proposed system. The results are presented in the next section.

3. Performance Evaluation

The performance of the proposed system has been evaluated with the available patient cases in BraTS datasets. The quality of the prediction of the tumor pixel distribution in a 3D brain image has been assessed. So has the quality of the brain tumor detection. The information about the datasets is found in Subsection 3.1. The performance measurements and ablation study are found in Subsection 3.2, and the performance comparison is presented in Subsection 3.3.

3.1 Dataset

The processing quality of the proposed system has been measured with the data of BraTS2021 [26]. There are 1251 patient cases of MRI scanning and each is accompanied by a ground-truth tumor mask approved by medical specialists. As the system does not need training, the data of all the 1251 patient cases have been used to measure the processing quality of both the prediction of the tumor pixel distributions and the brain tumor detection.

In BraTS2021 dataset there are additional 219 patient cases, referred to as the validation samples, of which the ground truth data is not accessible for public. They have also been used to evaluate the tumor detection quality of the proposed system, by means of the online platform Synapse [29] where the assessment is a standard process with data from the Cancer Imaging Archive [30-33].

In order to compare the performance of the proposed system, in terms of brain tumor detection, with those published in recent years, earlier versions of BraTS datasets, namely BraTS2013, BraTS2017, BraTS2018 [34], BraTS2019 [35] and BraTS2020 [36] have also been used for the evaluation. The number of patient cases in each of the datasets is specified in Table 1. In case of testing on the validation samples of these datasets, the tumor detection results have been evaluated by the online platform, Center for Biomedical Image Computing and Analytics Image Processing Portal (CBICA IPP) [37].

Table 1 Numbers of patient cases in BraTS datasets

	BraTS 2013	BraTS 2017	BraTS 2018	BraTS 2019	BraTS 2020	BraTS 2021
Training set	30	285	285	335	369	1251
Validation set	N.A.	N.A.	66	125	125	219

3.2 Performance Measurements

The quantitative measurements of the performance have been done mainly with the data of the 1251 patient cases of MRI scanning, including the ground truth data, in BraTS2021 dataset. In this subsection, the description of the performance metrics is found in Subsection 3.2.1, the results of the comprehensive tests of the prediction and detection in Subsection 3.2.2 and Subsection 3.2.3, respectively, and the ablation study in Subsection 3.2.4.

3.2.1 Performance Metrics

As the proposed system is designed to predict the gray level distributions of tumor pixels and to detect tumors, the performance metrics involve 2 kinds of measures, for the prediction and the detection, respectively.

The prediction quality can be measured by the degree of similarity between the predicted and true histograms. Correlation coefficient (CC), mean squared error (MSE) and structural similarity index measure (SSIM) [38] are commonly used for similarity measurement. SSIM is defined as follows.

$$\text{SSIM}(\mathbf{x}, \mathbf{y}) = [l(\mathbf{x}, \mathbf{y})]^\alpha \cdot [c(\mathbf{x}, \mathbf{y})]^\beta \cdot [s(\mathbf{x}, \mathbf{y})]^\gamma \quad (5)$$

where

$$l(\mathbf{x}, \mathbf{y}) = \frac{2\mu_x\mu_y + C_1}{\mu_x^2 + \mu_y^2 + C_1}, \quad c(\mathbf{x}, \mathbf{y}) = \frac{2\sigma_x\sigma_y + C_2}{\sigma_x^2 + \sigma_y^2 + C_2}, \quad s(\mathbf{x}, \mathbf{y}) = \frac{\sigma_{xy} + C_3}{\sigma_x\sigma_y + C_3}$$

(\mathbf{x}, \mathbf{y}) are two sets of data, (μ_x, μ_y) denote the mean values of \mathbf{x} and \mathbf{y} , (σ_x, σ_y) are the standard deviations, σ_{xy} is the correlation coefficient, (α, β, γ) are set to be (1, 1, 1), and (C_1, C_2, C_3) are small non-zero constants to stabilize the division with weak denominator.

The detection quality can be measured in Dice score indicating how much a predicted object mask and the true object mask are overlapped. It is defined as

$$\text{Dice}(X, Y) = \frac{2TP}{(TP+FN)+(TP+FP)} \quad (6)$$

where TP (true positive) is the overlapped part of the predicted and true object masks, FN (false negative) is the part of the true object mask that is not covered by the predicted mask. The entire true object mask is represented by $(TP + FN)$ and the predicted one by $(TP + FP)$.

Sensitivity (Sens) and false discovery rate (FDR) [39], defined as

$$Sens = \frac{TP}{TP+FN} \quad (7)$$

$$FDR = \frac{FP}{TP+FP} \quad (8)$$

can also be used to measure the detection quality, as complements to Dice score.

3.2.2 Prediction Results

To evaluate the prediction quality of the proposed system, the similarity between the predicted 2D histogram of the tumor pixels in each of the axial, coronal and sagittal series and its ground truth has been measured on the 1251 patient cases from BraTS 2021 dataset. Large varieties of tumors appear in these 1251 cases, and some are more difficult to detect than others. The test results, presented as statistic values of SSIM, CC and MSE measures, are shown in Table 2. The following two points are observed.

- Overall, the proposed system is able to deliver predicted 2D histograms of good quality, confirmed by the overall average SSIM of 84.3% and MSE of 0.004 on the 1251 cases.
- The median SSIM value of 2D histograms, obtained from axial, coronal or sagittal series, is visibly higher than the mean value, and even the 25-quantile is around 80%. It is confirmed that the proposed prediction method yields a good result for a large majority of patient cases.

Table 2 Similarity between the predicted and true gray level distributions. The data are generated by testing the 1251 patient cases of BraTS2021 dataset

		Predicted 2D gray level distributions of tumor pixels			Predicted CDF of tumor pixels
		Axial	Coronal	Sagittal	
SSIM	mean	0.841	0.837	0.851	0.944
	median	0.944	0.942	0.947	0.967
	25quantile	0.798	0.796	0.818	0.945
	75quantile	0.979	0.978	0.980	0.973
CC	mean	0.878	0.872	0.887	0.958
	median	0.956	0.954	0.958	0.971
	25quantile	0.856	0.855	0.874	0.960
	75quantile	0.982	0.981	0.983	0.974
MSE	mean	0.0049	0.0038	0.0028	0.0113
	median	0.0016	0.0013	0.0009	0.0027
	25quantile	0.0006	0.0005	0.0004	0.0007
	75quantile	0.0054	0.0041	0.0031	0.0101

The prediction results have been applied to detect brain tumor by means of a block with very simple thresholding and filtering operations. The test results of the tumor detection are presented in the following subsection.

3.2.3 Tumor Detection Results

As the proposed system does not need training, the data samples in both validation and training sets have been used to assess its quality of the brain tumor detection delivered by the proposed system. It is done in the following 2 approaches.

- Testing on the 3 validation sets from BraTS 2018, 2019, 2020 and 2021 datasets, respectively, as the validation sets of BraTS2019 and BraTS2020 are identical. Then using the online validation tools, namely CBICA IPP [37] and Synapse [29], to get the results.
- Testing on the 4 training sets from the same datasets and measuring the detection quality with the available ground truth data. The advantage of this approach is that the test is done on a large number of data samples. For example, one can test on the 1251 patient cases in the training set, instead of 219 in the validation set, of BraTS2021 dataset. Thus, the test has been done quite comprehensively.

In total, there are 7 tests, each on a different set of patient cases. The test results, measured in Dice score, Sensitivity and FDR, are summarized in Table 3, presented in 7 columns. One can see that, in all the columns, the mean Dice scores are higher than 0.80 and the median values are higher than 0.86. In the right-most column, given by the test performed extensively on the 1251 patient cases, the Dice scores of 25 quantile is 0.767, indicating that the Dice scores of 75% of the cases are 0.767 or more. It has been confirmed that the proposed detection method, applying the results of the predicted tumor pixel distributions, is very effective to detect most brain tumors, despite the vast variations in their locations, shapes, sizes and texture patterns in the tumor areas. The same test results are also visualized in Fig. 15 by means of boxplots.

It should be underlined that, as the parameters of the proposed system are not determined by training, neither the problem of randomness in training nor the problem of reproducibility could arise. Hence the performance is robust and reliable.

Table 3 Dice score, sensitivity and FDR of tumor detected by the proposed system

Flair mono-modality input	Test on validation set (assessed by online portal)			Test on training set				
	BraTS dataset	2018	2019/2020	2021	2018	2019	2020	2021
Number of patient cases	66	125	219	285	335	369	1251	
Dice	mean	0.843	0.816	0.812	0.814	0.816	0.818	0.802
	median	0.884	0.881	0.874	0.869	0.873	0.872	0.876
	25quantile	0.807	0.771	0.769	0.772	0.786	0.786	0.767
	75quantile	0.914	0.917	0.915	0.913	0.914	0.914	0.920
Sens	mean	0.850	0.819	0.824	0.825	0.835	0.834	0.827
	median	0.896	0.877	0.885	0.881	0.896	0.893	0.904
	25quantile	0.815	0.756	0.777	0.777	0.787	0.778	0.785
	75quantile	0.940	0.928	0.941	0.944	0.949	0.948	0.955
FDR	mean	0.127	0.138	0.154	0.150	0.154	0.150	0.162
	median	0.102	0.097	0.102	0.091	0.100	0.092	0.101
	25quantile	0.175	0.176	0.188	0.190	0.190	0.183	0.190
	75quantile	0.044	0.033	0.048	0.037	0.042	0.042	0.049

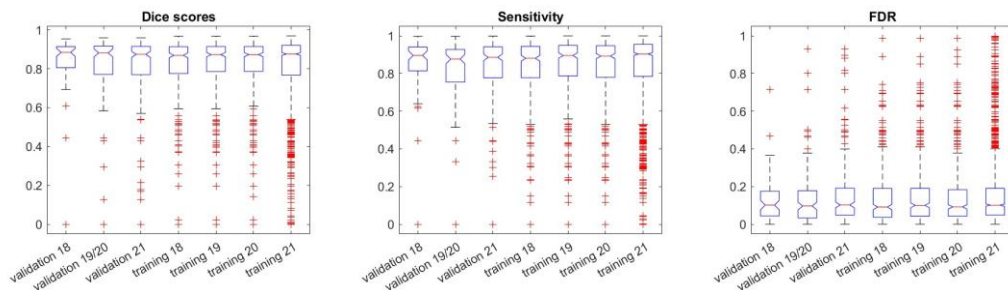


Fig. 15 Boxplots illustration of the results in Table 3. The tests have been done on 7 different sets of data samples.

3.2.4 Ablation Study

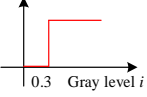
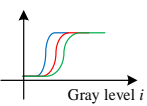
The proposed system, shown in Fig. 3, has 2 important characters for the prediction of the tumor pixel distribution and the tumor detection.

- Modulation of the asymmetry maps and the 2D histograms. The modulation functions are made adaptive to each patient case as they are generated from the original data of the case.
- Progressive prediction and cropping. The 3D data sample is cropped following each of the 3 coarse predictions of tumor pixel distribution. The final prediction is done after most of the tumor-free pixels are removed by the cropping operations.

The ablation study has been done by 2 trials related to the 2 characters. The 2 trials have been conducted with the data of all the 1251 patient cases of BraTS2021. The results comprise the similarity, measured in SSIM, between the predicted and true 2D histograms and Dice score of tumor detection.

The first trial is to test if the adaptability of the modulation functions f_{m1} and f_{m2} contribute positively to the performance of the proposed system. To this end, the system is modified by replacing f_{m1} and f_{m2} by a unit-step function $u(i-0.3)$, suppressing all the elements in the lower 30% gray level section, regardless the original pixel distributions. The test result of this modified system is presented in the first part of Table 4, in comparison with that of the proposed one. One can see a significant difference between the two, proving the effectiveness of the proposed adaptive modulation functions and the necessity to apply them to achieve a good processing quality in the prediction and the detection.

Table 4 Similarity (SSIM) of histogram prediction and Dice score of tumor detection obtained in the ablation study of Trial 1 and 2

Trials	#	Descriptions	Histogram, SSIM*				Tumor mask, Dice*
			Axial	Coronal	Sagittal	Mean	
Trial 1. Modulation of the 2D histograms	A	Step function $u(i-0.3)$ replacing the adaptive modulations 	0.777	0.775	0.785	0.779	0.762
	P	Proposed modulation functions $f_{m1}(i)$ and $f_{m2}(i)$ adapting to individual cases 	0.841	0.837	0.851	0.843	0.802
Trial 2. Prediction with or without cropping operations	B	No cropping	0.669	0.669	0.689	0.676	0.482
	C	Only first cropping	0.789	0.778	0.794	0.787	0.613
	D	First and second cropping	0.842	0.836	0.839	0.839	0.735
	P	Proposed (cropping in all the 3 dimensions)	0.841	0.837	0.851	0.843	0.802

*: Mean values obtained by testing the 1251 patient cases of BraTS2021

#: Experiment label

In the proposed system, the prediction is done step-by-step while the regions of non-interest, i.e., tumor-free regions, are cropped out progressively, improving the density of object information and prediction quality. Trial 2 has been conducted to prove the contribution of the cropping operations to the system performance. In this trial, the system is modified 3 times, resulting in 3 modified versions. In the first one, there is no cropping at all, in the second one only tumor-free axial slices are cropped out before the final prediction, and in the 3rd one there are only 2 cropping operations for axial and coronal slices, instead of 3 in the proposed system. The 3 versions have been tested and the results are presented in the second half of Table 4. One can see that, the more the tumor-free regions are cropped out, the higher information density in the data to be processed in the next step, and the better the quality for the prediction and the detection. The best result is evidently given by the proposed system with 3 cropping operations. The ablation study results are also visualized in Fig. 16.

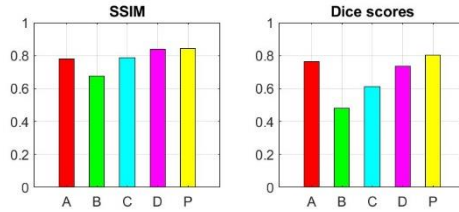


Fig. 16 Bar charts of the results of the ablation study performed on 5 different versions labelled A, B, C, D and P. The same results are presented in Table 4.

In summary, the results of the two trials in this ablation study confirm the essentiality and the effectiveness of the proposed modulation and the progressively predicting/cropping operations. These 2 operations combined make it possible to obtain a high-quality prediction and tumor detection by an extremely simple computation process.

3.3 Performance Comparison

The performance of the proposed system, in terms of detection quality, has been compared with that of other systems reported in reputed journals. As no data about the prediction of tumor pixel distributions are available, this performance comparison is in the aspect of brain tumor detection. To make the comparison meaningful, the test results of these systems should be produced, in principle, under the same conditions, i.e., testing on the same data samples and using the same performance metrics.

The comparison results of the proposed system with 2 non-CNN systems are presented in Table 5. These 2 systems were chosen for the comparison because their detection quality was assessed with BraTS datasets and the test conditions were the same as those of the proposed system.

Table 5 Comparison of the results of the proposed system with those of other non-CNN systems

Dataset	Systems	# cases for testing	Modality	Dice
BraTS 2013	Lim and Mandava 2018 [10]	20 ^H	T1c, T2	0.701
	Lim and Mandava 2018 [10]	10 ^L	T1c, T2	0.692
	Proposed	20^H	Flair	0.777
	Proposed	10^L	Flair	0.709
BraTS 2017	Bonte et al. 2018 [12]	210 ^H	Flair, T1c	0.762
	Bonte et al. 2018 [12]	75 ^L	Flair, T1c	0.656
	Proposed	210^H	Flair	0.829
	Proposed	75^L	Flair	0.772
BraTS 2021	Proposed	1251	Flair	0.802

H: High-grade glioma (HGG), L: Low-grade glioma (LGG)

Table 6 summarizes the comparison of the detection quality between the proposed system and 4 CNNs reported recently. In order to make the test results comparable to these CNN systems, the proposed system has been tested on BraTS 2018 and 2019 datasets, besides BraTS 2021 dataset. It should, however, be mentioned that, the test conditions of the proposed systems are much more rigorous, as the test has been done on all the available patient cases of each dataset, instead of a small number of cases sampled from the training pools of the datasets. Also, the test has been done on the BraTS validation sets and the Dice scores have been generated by a 3rd-party platform CBICA IPP [37], whereas the corresponding data of the other systems listed in the table are not available.

Table 6 Comparison of the results of the proposed system with those of CNN systems

Dataset	Systems	# cases for testing	Modality	Dice
BraTS2018 Training set	Wu et al. 2021 [3]	143 out of the 285	T2	0.619
	Zhou et al. 2021 [23]	57 out of the 285	Flair	0.737
	Yang et al. 2022 [24]	95 out of the 285	Flair	0.842
	Rahimpour et al. 2021 [25]	57 out of the 285	T1	0.790
	Proposed	All the 285 cases	Flair	0.814
BraTS2019 Training set	Zhou et al. 2021 [23]	67 out of 335	Flair	0.743
	Proposed	All the 335	Flair	0.816
BraTS2018 Validation set	Proposed	All the 66*	Flair	0.843
BraTS2019 Validation set	Proposed	All the 125*	Flair	0.816
BraTS2021 Training set	Proposed	All the 1251	Flair	0.802

* Testing on the official validation set, and the results are assessed by CBICA IPP [37]

The data presented in Table 5 and Table 6 demonstrate the high performance of the proposed system, specified in the following aspects.

- Processing quality measured in Dice scores. It outperforms the other systems, CNN or non-CNN, under the same or more tougher test conditions.
- Performance robustness and reproducibility. On one hand, the results of performance evaluation are obtained by testing extensively with a very large number of patient cases. They are much more comprehensive and reliable than those given by the other systems. On the other hand, as it is a deterministic system, its results are completely reproduceable.
- Computation cost. It is so low that one can run the computation procedure for the prediction and detection in an ordinary laptop or desktop. In case of laptop of i7-11800H CPU with clock of 4.6 GHz, it takes only 0.85 seconds to process a patient case.

It should be mentioned that the proposed system is developed analytically and the processing are modeled mathematically. The functions implemented in the system, such as the 2D histogram modulation or the gray level thresholding for the mask generation, are adaptive to the statistical image features of individual patient cases. Very little tuning is needed. Thus, users can be applied it easily, without "trial and error".

4. Conclusion

The challenges in brain tumor detection, like in all kinds of object detections, are often related to the extremely low density of object information in the input data and the enormous variations of the objects. In this paper, we have proposed a system that predicts the gray level distributions of tumor pixels, i.e., pixels in the tumor regions, of a 3D MRI brain scan of Flair modality, and detects precisely tumor locations in the 3D scan. We have proposed (i) 2D histogram presentations of the data in the axial, coronal and sagittal slice series of a 3D image, comprehending the distributions of the gray levels of the pixels with their locations, (ii) extraction of brain tumor information by exploiting the left-right asymmetry of a brain structure, (iii) histogram modulation, automatically on a case-by-case basis, to enhance the structural asymmetry related to the presence of tumors and to attenuate that due to non-pathological causes, (iv) step-by-step prediction of tumor pixel distribution, accompanied by step-by-step cropping out the areas of non-interest to improve the signal density, and (v) tumor mask generation process consisting of a simple thresholding, based on the prediction results, and a low-pass filtering for morphological purpose.

The proposed system does not need training. It has been tested extensively with the data of more than one thousand patient cases in BraTS 2018~2021 datasets. The test results demonstrate that, with the input data of only Flair modality, the predicted 2D histograms have a high degree of similarity with respect to the true ones. Also, the tumor detection performed by the system is also of high-quality. Moreover, as the system parameters are determined without randomness, its performance is completely reproduceable. It is worth mentioning that the good performance of the proposed system has been achieved at an extremely low computation cost that may be negligible with respect to those of other state-of-the-art systems.

Though the system has been designed to process the data of MRI brain scanning, it can also be used if the 3D data are from CT scanning. The design principle can also be applied to develop systems detecting 3D objects in a symmetrical environment.

Needless to say, the proposed system is not perfect. As it takes the input data produced by MRI Flair scanning to minimize the data volume in the process, its ability to identify some types of tumor regions, in particular in some low-grade glioma (LGG) cases, may be limited. Also, like many other existing systems, the performance may be reduced if the input images are of poor quality. The future work can be in 2 avenues. The first avenue is the input data pre-processing to improve the image quality. The other avenue is to incorporate CNN and knowledge-based processing blocks to further improve the processing quality. In this case, there will be new challenges of limitation of data samples and the risk of randomness in system training.

Acknowledgements

This work was supported in part by Digital Research Alliance of Canada and in part by the Natural Sciences and Engineering Research Council (NSERC) of Canada.

Reference

- [1] K. Simonyan, A. Zisserman, Very deep convolutional networks for large-scale image recognition, arXiv preprint arXiv:1409.1556 (2014). <https://doi.org/10.48550/arXiv.1409.1556>.
- [2] O. Ronneberger, P. Fischer, T. Brox, U-net: Convolutional networks for biomedical image segmentation, Proc. MICCAI (2015) 234–241. https://doi.org/10.1007/978-3-319-24574-4_28.
- [3] X. Wu, L. Bi, M. Fulham, D.D. Feng, L. Zhou, J. Kim, Unsupervised brain tumor segmentation using a symmetric-driven adversarial network, Neurocomputing 455 (2021) 242-254. <https://doi.org/10.1016/j.neucom.2021.05.073>.
- [4] M. Soltaninejad, G. Yang, T. Lambrou, N. Allinson, T.L. Jones, T.R. Barrick, F.A. Howe, X. Ye, Automated brain tumour detection and segmentation using superpixel-based extremely randomized trees in FLAIR MRI, Int. J. Comput. Assist. Radiol. Surg. 12 (2017) 183-203. <https://doi.org/10.1007/s11548-016-1483-3>.
- [5] T. Imtiaz, S. Rifat, S.A. Fattah, K.A. Wahid, Automated brain tumor segmentation based on multi-planar superpixel level features extracted from 3D MR images, IEEE Access 8 (2020) 25335-25349. <https://doi.org/10.1109/ACCESS.2019.2961630>.

- [6] G. Gilanie, U.I. Bajwa, M.M. Waraich, Z. Habib, H. Ullah, M. Nasir, Classification of normal and abnormal brain MRI slices using Gabor texture and support vector machines, *Signal Image Video Process.* 12 (2018) 479-487. <https://doi.org/10.1007/s11760-017-1182-8>.
- [7] W. Wu, A.Y.C. Chen, L. Zhao, J.J. Corso, Brain tumor detection and segmentation in a CRF (conditional random fields) framework with pixel-pairwise affinity and superpixel-level features, *Int. J. Comput. Assist. Radiol. Surg.* 9 (2014) 241–253. <https://doi.org/10.1007/s11548-013-0922-7>.
- [8] Z.U. Rehman, M.S. Zia, G.R. Bojja, M. Yaqub, J. Feng, K. Arshid, 2020. Texture based localization of a brain tumor from MR-images by using a machine learning approach, *Med. Hypotheses* 141, 109705. <https://doi.org/10.1016/j.mehy.2020.109705>.
- [9] K. Venkatachalam, S. Siuly, N. Bacanin, S. Hubálovský, P. Trojovský, An efficient Gabor Walsh-Hadamard transform based approach for retrieving brain tumor images from MRI, *IEEE Access* 9 (2021) 119078-119089. <https://doi.org/10.1109/ACCESS.2021.3107371>.
- [10] K.Y. Lim, R. Mandava, A multi-phase semi-automatic approach for multisequence brain tumor image segmentation, *Expert Syst. Appl.* 112 (2018) 288-300. <https://doi.org/10.1016/j.eswa.2018.06.041>.
- [11] M.T. Bennai, Z. Guessoum, S. Mazouzi, S. Cormier, M. Mezghiche, 2020. A stochastic multi-agent approach for medical-image segmentation: Application to tumor segmentation in brain MR images, *Artif. Intell. Med.* 110, 101980. <https://doi.org/10.1016/j.artmed.2020.101980>.
- [12] S. Bonte, I. Goethals, R.V. Holen, Machine learning based brain tumour segmentation on limited data using local texture and abnormality, *Comput. Biol. Med.* 98 (2018) 39-47. <https://doi.org/10.1016/j.combiomed.2018.05.005>.
- [13] H. Khotanlou, O. Colliot, J. Atif, I. Bloch, 3D brain tumor segmentation in MRI using fuzzy classification, symmetry analysis and spatially constrained deformable models, *Fuzzy sets syst.* 160 (2009) 1457-1473. <https://doi.org/10.1016/j.fss.2008.11.016>.
- [14] B.N. Saha, N. Ray, R. Greiner, A. Murtha, H. Zhang, Quick detection of brain tumors and edemas: A bounding box method using symmetry, *Comput. Med. Imaging Graph.* 36 (2012) 95-107. <https://doi.org/10.1016/j.compmedimag.2011.06.001>.
- [15] H. Su, D. Zhao, H. Elmannai, A. A. Heidari, S. Bourouis, Z. Wu, Z. Cai, W. Gui, M. Chen, 2022. Multilevel threshold image segmentation for COVID-19 chest radiography: A framework using horizontal and vertical multiverse optimization, *Comput. Biol. Med.* 146, 105618. <https://doi.org/10.1016/j.combiomed.2022.105618>.
- [16] A. Qi, D. Zhao, F. Yu, A. A. Heidari, Z. Wu, Z. Cai, Fa. Alenezi, R. F. Mansour, H. Chen, M. Chen, 2022. Directional mutation and crossover boosted ant colony optimization with application to COVID-19 X-ray image segmentation, *Comput. Biol. Med.* 148, 105810. <https://doi.org/10.1016/j.combiomed.2022.105810>.
- [17] K. Hu, L. Zhao, S. Feng, S. Zhang, Q. Zhou, X. Gao, Y. Guo, 2022. Colorectal polyp region extraction using saliency detection network with neutrosophic enhancement, *Comput. Biol. Med.* 147, 105760. <https://doi.org/10.1016/j.combiomed.2022.105760>.

- [18] X. Jiang, Y. Ding, M. Liu, Y. Wang, Y. Li, Z. Wu, 2023. BiFTransNet: A unified and simultaneous segmentation network for gastrointestinal images of CT & MRI, *Comput. Biol. Med.* 165, 107326. <https://doi.org/10.1016/j.combiomed.2023.107326>.
- [19] E. Başaran, 2022. A new brain tumor diagnostic model: Selection of textural feature extraction algorithms and convolution neural network features with optimization algorithms, *Comput. Biol. Med.* 148, 105857. <https://doi.org/10.1016/j.combiomed.2022.105857>.
- [20] A. Mondal, V. K. Shrivastava, 2022. A novel parametric flatten-p mish activation function based deep CNN model for brain tumor classification, *Comput. Biol. Med.* 150, 106183. <https://doi.org/10.1016/j.combiomed.2022.106183>.
- [21] Q. Ma, S. Zhou, C. Li, F. Liu, Y. Liu, M. Hou, Y. Zhang, 2022. DGRUnit: Dual graph reasoning unit for brain tumor segmentation, *Comput. Biol. Med.* 149, 106079. <https://doi.org/10.1016/j.combiomed.2022.106079>.
- [22] ASNR-MICCAI, Brain MR image synthesis challenge (BraSyn). <https://www.synapse.org/#!Synapse:syn51156910/wiki/622356>, 2023 (accessed 21st August 2023).
- [23] T. Zhou, S. Canu, P. Vera, S. Ruan, Latent correlation representation learning for brain tumor segmentation with missing MRI modalities, *IEEE Trans. on Image Process.* 30 (2021) 4263-4274. <https://doi.org/10.1109/TIP.2021.3070752>.
- [24] Q. Yang, X. Guo, Z. Chen, P.Y.M. Woo, Y. Yuan, D2-Net: Dual disentanglement network for brain tumor segmentation with missing modalities, *IEEE Trans. on Med. Imaging* 41 (2022) 2953-2964. <https://doi.org/10.1109/TMI.2022.3175478>.
- [25] M. Rahimpour, J. Bertels, A. Radwan, H. Vandermeulen, S. Sunaert, D. Vandermeulen, F. Maes, K. Goffin, M. Koole, Cross-modal distillation to improve MRI-based brain tumor segmentation with missing MRI sequences, *IEEE. Trans. Biomed. Eng.* 69 (2021) 2153-2164. <https://doi.org/10.1109/TBME.2021.3137561>.
- [26] RSNA-ASNR-MICCAI, Multimodal brain tumor segmentation challenge 2021 (BraTS2021). <http://braintumorsegmentation.org/>, 2021 (accessed 1st July 2022).
- [27] N. Geschwind, W. Levitsky, Human brain: left-right asymmetry in temporal speech region, *Science* 161 (1968) 186-187. <https://doi.org/10.1126/science.161.3837.186>.
- [28] Y. Sun, C. Wang, 2022. A computation-efficient CNN system for high-quality brain tumor segmentation, *Biomed. Signal Process. Control* 74, 103475. <https://doi.org/10.1016/j.bspc.2021.103475>.
- [29] RSNA-ASNR-MICCAI, Synapse platform. <https://www.synapse.org/#!Synapse:syn25829067/wiki/610863>, 2021 (accessed 6th September 2023).
- [30] B.H. Menze, A. Jakab, S. Bauer, J. Kalpathy-Cramer, K. Farahani, J. Kirby, et al, The multimodal brain tumor image segmentation benchmark (BRATS), *IEEE Trans. Med. Imaging* 34 (2015) 1993-2024. <https://doi.org/10.1109/TMI.2014.2377694>.

- [31] U. Baid, et al., The RSNA-ASNR-MICCAI BraTS 2021 benchmark on brain tumor segmentation and radiogenomic classification, arXiv:2107.02314, 2021. <https://doi.org/10.48550/arXiv.2107.02314>.
- [32] S. Bakas, H. Akbari, A. Sotiras, M. Bilello, M. Rozycki, J.S. Kirby, J.B. Freymann, K. Farahani, C. Davatzikos, 2017. Advancing the cancer genome atlas glioma MRI collections with expert segmentation labels and radiomic features, *Sci. Data* 4, 170117. <https://doi.org/10.1038/sdata.2017.117>.
- [33] S. Bakas, M. Reyes, A. Jakab, S. Bauer, M. Rempfler, A. Crimi, et al., Identifying the best machine learning algorithms for brain tumor segmentation, progression assessment, and overall survival prediction in the BRATS challenge, arXiv preprint arXiv:1811.02629 (2018). <https://doi.org/10.48550/arXiv.1811.02629>.
- [34] MICCAI, Multimodal brain tumor segmentation challenge 2018 (BraTS2018). <https://www.med.upenn.edu/sbia/brats2018/data.html>, 2018 (accessed 30th April 2018).
- [35] MICCAI, Multimodal brain tumor segmentation challenge 2019 (BraTS2019). <https://www.med.upenn.edu/cbica/brats2019/data.html>, 2019 (accessed 10th June 2019).
- [36] MICCAI, Multimodal brain tumor segmentation challenge 2020 (BraTS2020). <https://www.med.upenn.edu/cbica/brats2020/data.html>, 2020 (accessed 18th May 2020).
- [37] CBICA, Center for biomedical image computing and analytics image processing portal (CBICA IPP), <https://ipp.cbica.upenn.edu/>, 2017 (accessed 1st January 2018).
- [38] Z. Wang, A.C. Bovik, H.R. Sheikh, E.P. Simoncelli, Image quality assessment: from error visibility to structural similarity. *IEEE Trans. Image Process.* 13 (2004) 600-612. <https://doi.org/10.1109/TIP.2003.819861>.
- [39] Y. Benjamini, Y. Hochberg, Controlling the false discovery rate: A practical and powerful approach to multiple testing, *J. R. Stat. Soc. Series B Stat. Methodol.* 57 (1995) 289-300. <https://doi.org/10.1111/j.2517-6161.1995.tb02031.x>.